Local membrane ordering of sponge phases at a solid–solution interface

W. A. Hamilton[a)] and L. Porcar
Solid State Division, Oak Ridge National Laboratory, Oak Ridge, Tennessee 37831

Paul D. Butler[b)]
NIST Center for Neutron Research, National Institute of Standards and Technology, Gaithersburg, Maryland 20899

Gregory G. Warr
School of Chemistry, The University of Sydney, Sydney, NSW 2006, Australia

We report a study of the ordering of the surfactant membranes of cetylpyridiniumchloride–hexanol in heavy brine sponge phase solutions in the proximity of a quartz surface by simultaneous neutron reflectometry (NR) and ''near surface'' small angle neutron scattering (NS-SANS) measurement in a reflection geometry sample cell. The NR results indicate layered surface ordering correlated with the solid–solution interface and decaying exponentially with depth over distances corresponding to a few membrane separations. The absolutely normalized NS-SANS results are consistent with conventional bulk SANS measurements, also indicating that the layered ordering established very near the surface does not constitute a phase of significant volume. We have compared this local surface ordering with the dilution behavior observed for sponge and lamellar phases in the bulk. At low membrane volume fraction the surface layering periodicity corresponds to the bulk sponge correlation peak, but approaches the smaller periodicities measured for lamellar systems at the same membrane volume fraction at higher concentrations. © *2002 American Institute of Physics.*
[DOI: 10.1063/1.1469602]

I. INTRODUCTION

In many situations surfactants in solution organize themselves locally as bilayer membranes. Depending on the membrane curvature and interactions, these systems exhibit a wide variety of long range symmetries and physical characteristics. The most widely studied are certainly the distinctive L_α lamellar phases, which are typically refractive, highly birefringent and viscous. In a number of systems adjacent to the stability domain of the L_α phase, the very different L_3 membrane phases are observed.[1–3] In marked contrast to their neighboring phase, L_3 membrane phases are transparent, isotropic and free flowing. In scattering measurements these L_3 phases show no long range order, unlike the L_α phases for which sharp Bragg peaks indicate the regular stacking of bilayers with a well defined periodicity d_α. For L_3 phases a much broader correlation peak is observed. This suggests some less regular structure with a characteristic length $d_3 = 2\pi/Q_3$, where Q_3 is the correlation peak scattering vector.

On the basis of neutron scattering and electrical conductivity measurements Porte *et al.*[4] proposed that membranes in the L_3 phases of the cetylpyridiniumchloride(CPCl)–hexanol in brine system form a flexible bicontinuous spongelike structure.[5] In this morphology multiconnected curved surfactant membranes separate the brine solvent into two interpenetrating and equivalent subvolumes. The characteristic length d_3 is identified with the average pore or passage size of the sponge. Figure 1 shows sketches of the sponge and lamellar morphologies and a section of the phase behavior of the CPCl–hexanol in heavy brine system studied here as a function of the membrane volume fraction ϕ_M and the mass ratio of the membrane constituents, hexanol and CPCl. The sponge phase region exists over a narrow range of hexanol to CPCl ratios, but extends over wide range of membrane volume fractions exhibiting pore sizes from a few tens to several thousands of Å.

As we can see from Fig. 1, the isotropic sponge phase is of necessity a bulk phase. Its convoluted morphology could not be fully accomodated in the proximity of a surface or boundary, while the nearly flat membranes of the nearby lamellar phase would stack easily at such an interface. One might therefore expect such contraints would lead to departures from bulk phase equilibria due to locally significant surface contributions to the free energy.[6] In the present study we have used a combination of simultaneous neutron reflectometry (NR) and ''near surface'' small angle neutron scattering (NS-SANS) measurements in comparison with conventional bulk SANS to investigate how semi-infinite bulk sponge phases accommodate structurally to the ordering potential exerted by a single isolated surface.

To our knowledge, the only previous direct work on sponge phase solutions at interfaces at length scales comparable to those investigated here are studies on AOT surfactant systems in the rather more severely constrained geometry of the surface forces apparatus (SFA). In these studies

---

[a)]Author to whom correspondence should be addressed. Electronic mail: HamiltonWA@ornl.gov
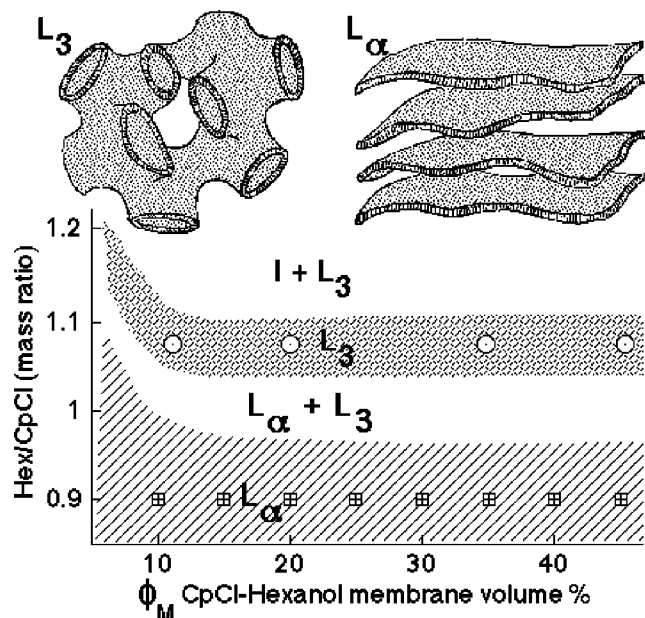[b)]Current address: Solid State Division, Oak Ridge National Laboratory, Oak Ridge, Tennessee 37831.

FIG. 1. Sketch views of the morphologies of the convoluted L_3 sponge phase and the simpler L_α lamellar phase for membrane systems, and a section the phase diagram for the CPCl–hexanol in heavy brine (0.2 M NaCl in D_2O) system with respect to membrane volume fraction ϕ_M, and the mass ratio of hexanol to CPCl. A biphasic, $L_\alpha + L_3$, region exists for mass ratios between those of the shaded pure L_α and L_3 phase regions. At mass ratios above that of the sponge phase a multiphasic $L_3 + I$("isotropic") region is observed. The dotted circles indicate the positions on the phase diagram of the sponge phases samples at a constant hexanol to CPCl mass ratio of 1.075, for $\phi_M = 11$, 20, 35, and 46 vol % studied by NR/NS-SANS and SANS. The crossed squares correspond to the lamellar phase samples ($m_{Hex}/m_{CPCl} = 0.9$) for the series $\phi_M = 10$, 15, 20, 25, 30, 35, 40, and 45 vol % measured by SANS to which the sponge results are compared in Sec. V.

Petrov *et al.*[7] and Antelmi *et al.*[8,9] observed oscillations and jumps in compressibility as the distance between two sponge solution confining mica surfaces was varied. At closest approach Antelmi *et al.* observed a decrease in the periodicity of these variations which they interpreted as confinement induced L_3 to L_α phase transition. In a previous NR study of disordered bicontinuous microemulsions, a system topologically similar to the sponge, Zhou *et al.*[10] reported layered structures at a free solution surface which extended to a depth of a few correlation lengths. Taken together these results strongly suggested that surface induced structures should be expected for sponge phases under the constraint of a solid–solution interface.

II. EXPERIMENT

The NR technique uses the specularly reflected beam to probe correlated surface structures within a depth range ~5000 Å of an interface. (General reviews of specular neutron reflectometry are given by Russell[11] and by Penfold and Thomas.[12]) This is commensurate with both the length scales most strongly characterizing the sponge phase, its pore size and pore–pore correlation length, and the corresponding lamellar phase spacing and correlations at the same volume fraction. The NR/NS-SANS technique presented here uses the small angle scattering from the beam transmitted into the

bulk in NR measurements to simultaneously monitor the bulk structure below the interface. The "near-surface" qualifier reflects that in these measurements beams are at grazing incidence to the quartz-solution interface ($\sim 1°$) and solution penetration depths are only a cm or so, the NS-SANS signal represents scattering from depths of only ~ 1–$100~\mu m$ into the solution.

Our group has used NS-SANS to investigate ordering induced in threadlike micellar systems at an interface by Poiseuille shear flow past a solid surface.[13–18] In those studies comparison of NS-SANS and conventional bulk SANS Couette shear measurements allowed the identification of mesoscopic flow-induced organization in the near-surface region distinct from the bulk structure.[16] In the case of the sponge systems measured here under static conditions it would allow the detection of similar effects near the interface, such as surface-induced nucleation or condensation of mesoscopic lamellar phase domains on the quartz surface. These could easily extend tens of μm beyond the surface and the range of NR without, by reason of membrane alignment or small effective sample volume, being evident in conventional bulk SANS measurements.

The reflection geometry solid–solution interface cell used in our measurements is shown schematically in Fig. 2(a). In this cell the sample solution sits in a rectangular trough 1 mm deep by 25 mm wide extending 80 mm (L) of the 82.5 mm length (L_Q) of a 12 mm thick slab of polished crystalline quartz. The trough is sealed with a Teflon O-ring seated in the cell's stainless steel base. This static cell is similar to a larger one used previously in the Poiseuille sheared solution measurements, so the cell's general design principles[14] and overall off-specular scattering geometry[13,15] have been described in detail elsewhere. The NR/NS-SANS measurements were taken on the neutron reflectometer MIRROR on the HB3A beamline of the High Flux Isotope Reactor at Oak Ridge National Laboratory.[19,20] In these measurements MIRROR's operating wavelength was $\lambda = 2.59$ Å ($\delta\lambda/\lambda \sim 1\%$) corresponding to a wave vector $k = 2\pi/\lambda = 2.43$ Å^{-1}. Neutrons entered the instrument through a slit 0.22 mm wide in the $\hat{z}$ direction located 0.95 m from the sample position and passed into the quartz slab to meet the quartz-solution interface at grazing incidence (angle α_i). A loose guard slit allowed the full length of the sample cell to be exposed to the neutron flux. Precisely positioned absorbing cadmium barriers meeting the quartz at the ends of the solution trough ensure that neutrons reaching the detector beyond the cell are either: (i) specularly reflected at the quartz-solution interface exiting at a grazing angle $\alpha_f = \alpha_i$, corresponding to a specular scattering vector normal to the interface ($\hat{z}$) of magnitude $Q_R[\alpha_i] = 2k\sin\alpha_i$; or (ii) have undergone transmission into the solution followed by scattering event in the solution deflecting them back toward the solution–quartz interface through which they are again transmitted.

The MIRROR instrument is equipped with a translation stage mounted one-dimensional linear position sensitive detector[21] positioned 3.42 m downstream from the sample. This allows measurement of both specularly reflected neutrons and off-specularly scattered neutrons near the reflection
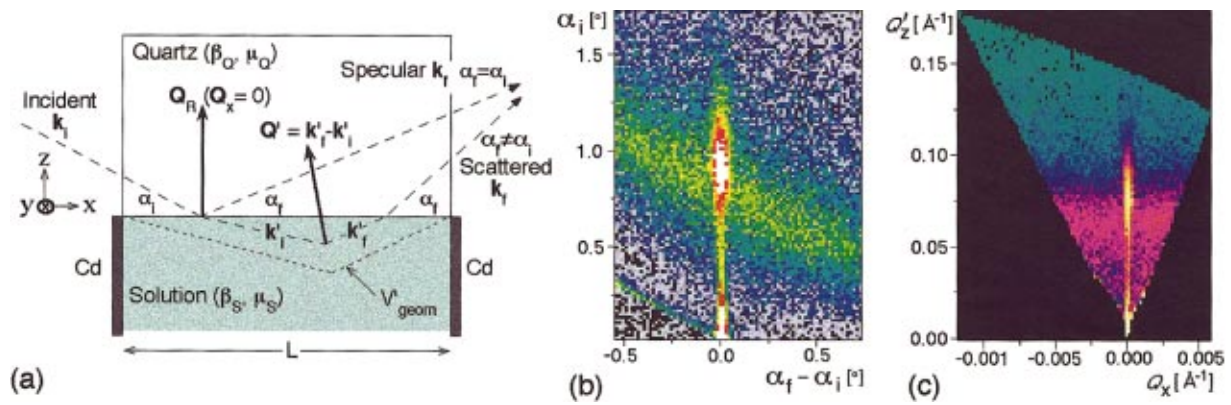
FIG. 2. (Color) (a) Schematic of the reflection geometry NR/NS-SANS cell used in our experiments indicating the geometry of incident, reflected and NS-SANS scattered wave vectors as designated in the text. The vertical scale has been exaggerated for clarity. (b) NR/NS-SANS data for the 35 vol % sponge sample. For each of the individual position sensitive detector scans (horizontal) at the incident beam grazing angle α_i the position on the detector has been converted to the off-specular angle $\alpha_f = \alpha_i$. The NR signal runs vertically at the specular position, $\alpha_f - \alpha_i = 0$. The most prominent NS-SANS signal runs diagonally across the data set approximately at constant angle to the direct beam position $\alpha_f - \alpha_i = -2\alpha_i$. (c) The 35 vol % sponge NR/NS-SANS data normalized to the sample's NS-SANS scattering volume corrected for absorption and transformed from angular coordinates $(\alpha_i, \alpha_f - \alpha_i)$ to reflection plane scattering coordinates (Q_x, Q_z').

plane defined by the incident and reflected scattering vectors $(\hat{x}, \hat{z})$. In our NR/NS-SANS measurements the detector is translated in the $\hat{z}$ direction to track the reflected beam as the sample angle changes. Its active length in the reflection plane $(\hat{z})$ is 100 mm at 0.93 mm per binning pixel, while each pixel has an active width in the transverse direction $(\hat{y})$ of 50 mm. The consistent analysis of NR/NS-SANS data taken in the geometry presented here allows a more reliable subtraction of NS-SANS backgrounds to specular reflection measurements, thus improving the accuracy of NR determinations of interfacial structures.

On each pass through the interface the neutron beam will be refracted if the neutron scattering length density of the solution β_S differs from that of the quartz β_Q.[15,22] For the NS-SANS signal this means that the measured off-specular scattering component normal to the interface, $Q_z = k(\sin\alpha_f + \sin\alpha_i)$, must be corrected for refraction to obtain the true normal component of the scattering vector in terms of in-solution beam grazing angles, α_i' and α_f' (denoting in-solution quantities by primes),

$$Q_z' = k(\sin\alpha_f' + \sin\alpha_i')$$
$$= k(\sqrt{\sin^2\alpha_f - \sin^2\alpha_c} + \sqrt{\sin^2\alpha_i - \sin^2\alpha_c}) \quad (1)$$

where α_c is the critical angle for total external reflection at the interface $[\sin^2\alpha_c = \lambda^2(\beta_S - \beta_Q)/\pi)]$. Scattering vector components parallel to the interface $(\hat{x}, \hat{y})$ are not effected by refraction, so for the $\hat{x}$ component along the interface in the reflection plane we may use the normal small angle approximation,[23,24]

$$Q_x' \equiv Q_x = k(\cos\alpha_f - \cos\alpha_i) \cong Q_z(\sin\alpha_i - \sin\alpha_f)/2$$
$$\cong Q_z'(\sin\alpha_i' - \sin\alpha_f')/2. \quad (2)$$

Due to the small size of the angular term in this transform Q_x is about two orders of magnitude smaller than Q_z and Q_z' in our scans. For a given Q_z' (i.e., $\sin\alpha_i' + \sin\alpha_f' \equiv 2\sin\alpha_z'$) the

conditions of entrance and exit from the solution allow Q_x' to be measured over a limited range $(-Q_z'\sin\alpha_z', Q_z'\sin\alpha_z')$.

From Fig. 2(a) we can see that a conventional SANS camera detector would be oriented in the $(\hat{y}, \hat{z})$ plane. As noted above the specularly reflected beam width determined with the detector in the $\hat{y}$ orientation was 42 mm FWHM (18 mm rms). Since the specular beam has a zero Q_y transfer, this width considered as scattering from the sample position 3.42 m upstream determines the intrinsic Q_y resolution of the scattering measurement (equivalently it is the $\Delta Q_y = 0$ response). In the detector's usual NR/NS-SANS $\hat{z}$ orientation this will be convoluted with the 50 mm detector $\hat{y}$ pixel width (14 mm rms), giving a transverse angular resolution of 6.7 mrad rms. At the operating wavelength in these measurements, 2.59 Å, this corresponds to $\delta Q_y = 0.016$ Å^{-1}.[25] The detector's 0.93 mmm pixel width gives the instrument an intrinsic resolution in the $\hat{z}$ direction that is over an order of magnitude better, $\delta Q_z \sim 0.001$ Å^{-1}. While, due to the small size of the angular term in the Q_x transform, Eq. (2) above, the resolution in the $\hat{x}$ direction is about two orders of magnitude better again $\delta Q_x \sim 10^{-5}$ Å^{-1}. The relatively poor resolution in Q_y means that the effective in-solution scattering vector corresponding to a particular pixel in the NS-SANS data set is given by

$$Q \cong \sqrt{Q_x^2 + (\delta Q_y)^2 + Q_z'^2}. \quad (3)$$

Inclusion of the $(\delta Q_y)^2$ term provides a first order correction to the effect on the scattering vector of the poor resolution in the $\hat{y}$ direction (the much smaller contributions from resolution in the other directions are negligible). This correction to the scattering vector, which is a rms averaging of the possible scattering vectors contributing to the NS-SANS signal at each detector pixel, is adequate in the current situation since the isotropic bulk scattering we observe varies relatively slowly with Q over the measured range.

The NR/NS-SANS measurements were performed for four bulk sponge phase samples of CPCl–hexanol (in mass ratio $m_{Hex}/m_{CPCl}=1.075$) in heavy brine (0.2 M NaCl in D_2O, Debye screening length 6.8 Å) at nominal membrane volume fractions of 11, 20, 35, and 46 vol %. (The respective membrane volume fractions calculated from mass fractions and CPCl and hexanol molecular volumes were 11.1, 20.0, 34.8, and 45.6 vol %.) The positions of these samples on the phase diagram are shown as circled points in Fig. 1. In all cases they are well within the boundaries of the sponge phase region.[26]

Figure 2(b) shows the NR/NS-SANS data scan for the 35 vol % sponge sample before full reduction with respect to the sample scattering parameters. Each horizontal row of pixels represents the position sensitive detector signal after the subtraction of a shutter closed instrument background, correction for detector efficiency, and normalization to the instrument's beam monitor count. The vertical axis of the data set is the neutron beam's grazing angle of incidence, α_i. Since the MIRROR's detector tracks the strong specularly reflected signal it stays at the same position on the detector at $\alpha_f-\alpha_i=0$ on the horizontal axis. The major feature in the reflected signal is a clear peak when $\alpha_i\simeq0.85°$ ($Q_R\simeq0.075$ Å^{-1}).

For an incident angle of α_i the direct beam would be at an apparent exit angle of $-\alpha_i$ (i.e., in data set coordinates $\alpha_f-\alpha_i=-2\alpha_i$). To reduce background and avoid damage to the detector most of the intense direct beam is blocked by a shade beyond the sample cell, but the edge of the beam above the shadow region and some signal leakage due to air scattering can be seen as a narrow diagonal stripe just above the true direct beam position in the lower left corner of the data set. For this sample the solution and quartz are nearly contrast matched ($\beta_S\cong\beta_Q$), so there is little refractive distortion. Features parallel to this stripe are therefore at constant angle to the direct beam, and consequently at constant Q_z. At this angle a strong band of NS-SANS signal is observed crossing the central region of the data set. Its intersection with the reflected beam is at a noticeable offset to the specular peak, clearly indicating a bulk solution periodicity different from that of the local surface structure causing the specular feature.

For NS-SANS the total volume of scattering that contributes to the signal is strongly dependent on the in-solution scattering angles. The geometrically possible scattering volume is a wedge of the incident beam width W and triangle defined by the quartz–solution interface and the limiting beam paths for neutron entry into the solution at angle α_i' immediately past the leading cadmium barrier and exit at an angle α_f' just above the trailing cadmium barrier. These extremum beam paths are indicated in Fig. 2(a). This limits the geometrically possible volume to

$$V_{geom}'=WL^2/2(\cot\alpha_i'+\cot\alpha_f'). \quad (4)$$

The actual effective scattering volume in NS-SANS has the same angular dependence as the geometric volume, but is corrected for absorption.[15,16] So,

$$V_S'\cong V_{geom}'e^{-\mu_Q L_Q}\frac{2((\mu_S-\mu_Q)L-1+e^{-(\mu_S-\mu_Q)L})}{(\mu_S-\mu_Q)^2 L^2}, \quad (5)$$

where μ_Q and μ_S are the absorption coefficients of the quartz and solution, respectively. The sample absorption dominates this correction. From transmission measurements at 2.59 Å the values of μ_S for the 11, 20, 35, and 46 vol % samples were determined to be 1.13, 1.53, 2.18, and 2.56 cm^{-1}, respectively, while that for the crystalline quartz slab is rather lower $\mu_Q=0.04$ cm^{-1}. These values are high enough that for all our samples the effective sample volume is less than 10% of the geometrically possible volume. For $(\mu_S-\mu_Q)L\gg1$ and $\mu_S\gg\mu_Q$ we may estimate the effective depth of penetration for the NS-SANS scattering volume as

$$D_{eff}\sim1/\mu_S(\cot\alpha_i'+\cot\alpha_f'). \quad (6)$$

For negligible refraction the effective depth probed by the NS-SANS background signal at the specular reflection angle is then $D_{eff}\sim\alpha_i/2\mu_S$. For the data presented in Figs. 2(b) and 2(c) ($\mu_S=2.18$ cm^{-1}) this varies from about 1 μm in the first detector scan ($\alpha_i=0.03°$) to about 60 μm at the maximum angle of incidence ($\alpha_i=1.7°$).

For small angles we may approximate the angular dependence of the NS-SANS sample volume from Eq. (4) by

$$1/(\cot\alpha_i'+\cot\alpha_f')\cong\alpha_i'\alpha_f'/(\alpha_i'+\alpha_f')$$

$$\cong\alpha_i'(1-\alpha_i'/2\alpha_z'). \quad (7)$$

So at a given Q_z' the NS-SANS sample volume has an inverted parabolic angular dependence. It is zero for $\alpha_i'=0$ and $\alpha_i'=2\alpha_z'$ (i.e., $\alpha_f'=0$) and a maximum in the symmetric condition when $\alpha_i'=\alpha_f'=\alpha_z'$, i.e., for in-solution scattering which will appear at the same final scattering vector as the specularly reflected beam. This leads to a symmetric intensity falloff in the NS-SANS signal at a given Q_z' (or α_z') with increasing angular separation from the specularly reflected signal.

Figure 2(c) shows a mapping of the 35 vol % data set shown in Fig. 2(b) after correction for the angular dependence of the NS-SANS scattering volume and transforming from angular coordinates ($\alpha_i,\alpha_f-\alpha_i$) to reflection plane scattering coordinates (Q_x,Q_z'). In the off-specular region where this correction applies the NS-SANS cross section for this system is seen to be essentially constant over the narrow range of Q_x covered for a given Q_z'. This partially normalized signal also now shows a more gradual falloff a low Q_z' from a peak shoulder at $Q_z'\sim0.065$ Å^{-1}. The steeper falloff in the measured off-specular scattering signal strength at low angle in Fig. 2(b) is a consequence of a small effective sample volume at small incident and exit angles, i.e., large $\cot\alpha_i'$ and $\cot\alpha_f'$.

Full reduction of the NS-SANS signal regions of the data sets, correcting for refraction, effective sample volume, and quartz–solution interface transmission, allows us obtain the macroscopic differential cross section for the near surface region of the solution. In determinations of the specular reflectivity from our samples the NS-SANS signal is a background signal. Since this signal cannot be measured directly in the specular region it must be estimated from off-specular measurements. Using the known scaling of the NS-SANS
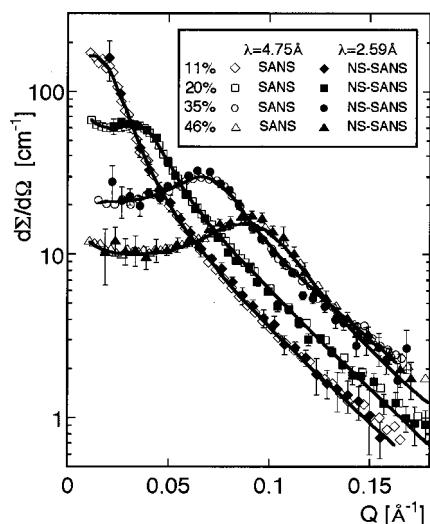
FIG. 3. Comparison of fully reduced NS-SANS data (plotted as full symbols) and corresponding bulk SANS measurements (open symbols) for the 11, 20, 35, and 46 vol % sponge samples. Macroscopic cross section $d\Sigma_S/d\Omega$ vs scattering vector Q. Fits to the bulk SANS data are shown as solid lines.

signal presented above allows improved estimation of this scattering background contribution. Note that the NS-SANS signal corrections themselves involve transmission factors which are determined from the specular reflectivity. Thus this full reduction of the data sets is necessarily an iterative procedure, beginning from initial signal estimates. Iterative reduction is particularly important in order to obtain good results at low scattering vectors, where transmission variation and angular dependence of the scattering will have the strongest effects on initial NR and NS-SANS signal estimates. The simultaneous reduction of the NR/NS-SANS data has the further advantage that the NS-SANS cross sections may be absolutely normalized against easily determined NR cross sections. Below the critical angle for total reflection the latter depend only on geometric factors and the quartz slab transmission which cancels with the common term in the NS-SANS signal. The procedure we used to obtain the fully reduced NR and reflection plane NS-SANS data for the current instrument geometry is outlined in Appendix A.

III. NS-SANS AND SANS DATA ANALYSIS

Figure 3 shows the fully corrected reflection geometry NS-SANS determination of the differential scattering cross sections for our series of samples on the MIRROR reflectometer at $\lambda = 2.59$ Å data (full symbols) binned against the in-solution scattering vector Q as determined from Eq. (3). They are shown in comparison with conventionally measured and corrected bulk SANS measurements on the same solutions made on the ORNL SANS instrument[27] at $\lambda = 4.75$ Å (open symbols). The absolute normalization uncertainty for the conventional SANS measurements is $\pm4\%$, typical of such measurements. Due to the more complicated geometry and absorption corrections the uncertainties for the NS-SANS measurements are somewhat larger $\sim 10\%$. (This is discussed in detail in Appendix B.)

As Fig. 3 shows corresponding measurements in the SANS and NS-SANS series agree within these levels of absolute cross-section accuracy throughout the commonly measured Q ranges. This simple comparison of the data from these two instrumental geometries and wavelengths of itself indicates that there is no apparent shift of the lamellar (or biphasic) phase boundary in the bulk due to the presence of the solid interface and certainly no significant nucleation of the lamellar phase at the surface.

The structure factor in our fits to the SANS signal (solid lines in Fig. 3) was that used by Lei et al.[28] in their small angle x-ray study of sponge phases in the quaternary sodium dodecyl sulphate–water–pentanol–dodecane system,

$$S[Q] = 1 + \frac{A\,\arctan(Q\xi_{io}/2)}{Q} + \frac{B}{1 + (Q - Q_3)^2 \xi_3^2}. \qquad (8)$$

The final Lorentzian term describes the pore–pore correlation with correlation length ξ_3 and an average pore size $d_3 = 2\pi/Q_3$. This modifies the structure factor calculated by Roux et al.[29,30] describing the structure on length scales much larger than the pore size in terms of the characteristic "inside–outside" order parameter, ξ_{io}, of the solvent volumes separated by the membrane. We found ξ_{io} to be effectively infinite over the Q range probed in our experiments (as did Lei et al. in x-ray measurements reaching scattering vectors an order of magnitude lower than those accessible here). So this term in the structure factor appears as a simple A/Q in our fits. In all cases it made only a very small contribution in the region of the pore–pore correlation peak position.

The form factor used was a relatively simple analytic approximation to the scattering from a randomly oriented discoid of the CPCl–hexanol membrane's neutron contrast thickness for this system, $t_o = 20.5$ Å (see discussion in the next section) and transverse radius of gyration ρ. Its derivation was inspired by the fact that the form factor used by Lei et al., the average over random orientations of a disc of fixed radius R and contrast thickness t_o, could only be calculated numerically. Testing over the Q range covered in the measurements presented here (and somewhat beyond) the two forms were found to be essentially equivalent at the same transverse radius of gyration, i.e., when $R = \sqrt{2}\rho$ as expected. While use of the analytic form greatly reduced the data fitting times, for the purposes of comparison with the simultaneously collected NR measurements, the important parameter derived from the SANS data is the pore size d_3. This value is derived from the Lorentzian term in the structure factor and is relatively insensitive to the exact form factor. The expression and its derivation are therefore presented in Appendix C.

The three structural parameters (d_3, ξ_3, and ρ) obtained from the SANS fits are presented in Table I. In all cases the SANS values agree with (the less precisely determined) values obtained from the NS-SANS data. The d_3 value for the 11 vol % solution is an exception since the NS-SANS data in this case does not extend to low enough Q to allow an accurate determination of this parameter.

TABLE I. Fitting parameters derived from SANS and NR fits.

Sample ϕ_M (vol %)	SANS fit parameters[a]			NR fit parameters[b]							
	$d_3 = 2\pi/Q_3$ (Å)	ξ_3 (Å)	ρ (Å)	ϕ_M (vol %)	ϕ_s (vol %)	$\Delta\phi_M$ (vol %)	z_o (Å)	d_z (Å)	ξ_z (Å)	d_3/d_z	ξ_z/d_z
11 (11.1)	333 ± 25	103	23	11 ± 3	100	9.2	216 ± 15	326 ± 12	215	1.02 ± 0.08	0.65
20 (20.0)	171 ± 7	60	21	20 ± 3	100	14	124 ± 5	165 ± 3	109	1.04 ± 0.04	0.66
35 (34.8)	94 ± 3	52	11	35 ± 3	95	29	71 ± 3	83 ± 2	91	1.12 ± 0.04	1.10
46 (45.6)	71 ± 2	32	6.2	47 ± 3	94	42	55 ± 3	57 ± 2	126	1.22 ± 0.05	2.21

[a]All values given are derived from bulk SANS data, but give satisfactory fits to the NS-SANS data. Values consistent within larger errors may be derived directly from the NS-SANS data. The d_3 value for the 11 vol % solution is an exception since the NS-SANS data does not extend to low enough Q to allow an accurate determination.

[b]The repeatability accuracy of the MIRROR reflectometer in direct and reflected beam position determinations and hence angular calibrations is ~0.2 mm. For the instrument's 3.42 m sample to detector distance and 2.59 Å operating wavelength this corresponds to an absolute scattering vector uncertainty δQ_R ~0.0004 Å^{-1}. This contribution which dominates at low values of Q_R (i.e., for larger scale structures and critical reflection edge determinations) has been included in the uncertainty estimates of the NR derived parameters given in this table.

IV. NR DATA ANALYSIS

Figure 4 shows the series of specular reflection measurements for the four sponge samples (symbols). Also shown on these plots (dashed lines) is the extrapolated NS-SANS background subtracted from the specular beam region at each Q_R. This signal has been normalized as a specular signal [see Appendix A, Eq. (A1)] and therefore represents the effective specular reflection contribution of the background. Obviously this signal could overwhelm the true specular reflection signal near the correlation peak of the NS-SANS signal from the sponge and as $R[Q_R]$ falls at higher Q_R. In practice for the present case we were able to obtain statistically valid specular reflection measurements for signal to NS-SANS background ratios above ~1/3. In order to improve statistics in poor signal to background ratio regions of the data, it was necessary to rebin the measured data over several sequential incident angle steps. This is apparent in the broader rms resolution of Q_R at these values (shown as horizontal error bars).

Fits to the specular reflection signal are shown as solid lines, with the fitting scattering length density profiles as insets. Satisfactory fits were obtained with the following simple profile model. The quartz superstrate's scattering length density was fixed at the value of $\beta_Q = 4.17 \times 10^{-6}$ Å^{-2}. The bulk scattering length density of the solution was modeled by evenly displacing some volume fraction of the heavy brine $\beta_{D_2O} = 6.40 \times 10^{-6}$ Å^{-2} with material of scattering length density of $\beta_M = -0.05 \times 10^{-6}$ Å^{-2}, the averaged scattering length density of the hexanol to CPCl mix in our sponge samples. So the bulk sponge scattering length is given by

$$\beta_S = \phi_M \beta_M + (1 - \phi_M)\beta_{D_2O}. \qquad (9)$$

The bulk volume fraction of membrane, ϕ_M, was a free parameter in the fit. Using Eq. (9) and the values given above the contrast matched condition between the quartz and the bulk solution occurs for $\phi_M = 34$ vol %. A critical edge for total external reflection allowing absolute normalization of the NR/NS-SANS data sets is observed for the two samples below this concentration (11 and 20 vol %) and we note again that the 35 vol % sample is almost exactly contrast and refraction matched to the quartz.

Since the quartz surface is negatively charged and our system is cationic we expect an adsorbed membrane on the quartz surface.[31] The significant neutron scattering contrast from such a membrane will come primarily from its core, the hydrocarbon tails of CPCl and hexanol. SANS form factor measurements performed by our group gave a value for this membrane core thickness of $t_o = 20.5 \pm 1.0$ Å,[32] which is consistent with prior determinations for this system.[33,34] Dilution law determinations of the full membrane thickness, t_M, by our group (described in Sec. V and Appendix D) give a value of 25.6 ± 0.5 Å and are consistent with previous determinations for this system.[34,35] These values of the full thickness and the core width give a physically realistic estimate of about 2.5 Å for the surfactant head group layer thicknesses at the membrane surfaces. In order to limit the number of free fitting parameters we made no attempt to model the fine structure of the surface layer, such as the weaker neutron contrast of these molecular head groups outside the core. In any case, these would only contribute significantly to the signal at Q_R values higher than those covered in our measurements. Our NR fitting model's simplified surface layer therefore has only a fixed hydrocarbon thickness of $t_o = 20.5$ Å.

For the scattering length density of this surface layer we used a fixed value of -0.4×10^{-6} Å^{-2}, calculated from the molecular volumes of the tails, their scattering lengths and the hexanol to CPCl mixing ratio. The center of the layer was set at a fiducial depth $z = 0$. The free parameter for this part of the model was the volume occupation of the adsorbed layer in this region, ϕ_s. We were not able to fit the reflectivity data without including such a layer; and, as the scattering length density insets in Fig. 4 show, in all cases ϕ_s is nearly unity, as the scattering length density in this surface layer is close to -0.4×10^{-6} Å^{-2} for all the data set fits. The previously measured 3 Å rms surface roughness off our quartz surfaces was allowed for in the model by a fixed 3 Å Gaussian smearing of the fully developed profile. The effect
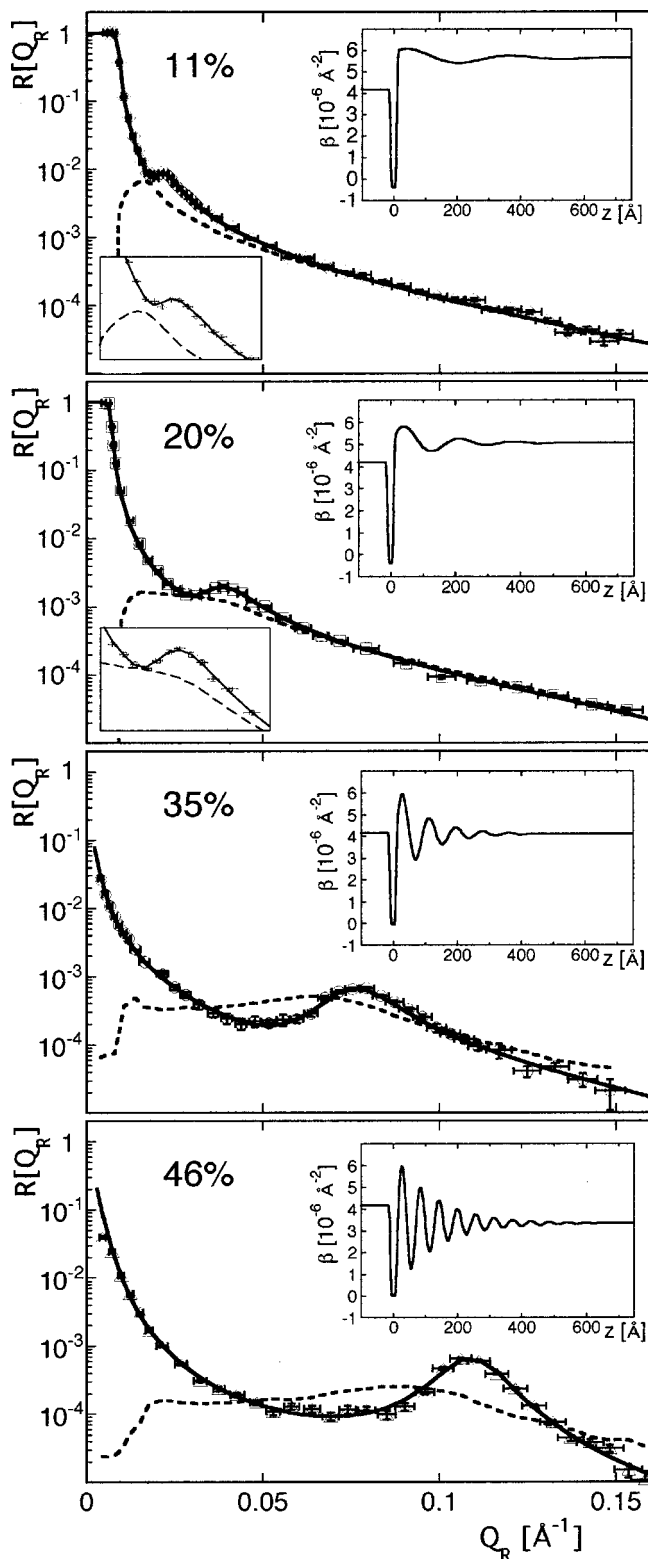
FIG. 4. NR measurements for the 11, 20, 35, and 46 vol % sponge samples (symbols). Specular reflection coefficient R vs specular scattering vector Q_R. The dashed lines show the extrapolated NS-SANS background subtracted from the specular beam region at each Q_R in the reduction procedure. Solid line fits are calculated from the scattering length density profiles shown in the insets in the upper right of each reflectivity plot. For the 11 and 20 vol % data sets an expanded view of the fit in the region of the local peaks in the reflection signal due to the surface ordering is shown in insets at bottom left.

of this smearing on the profile is visible at the boundaries of the surface layer and acts in a similar manner to a Debye–Waller factor throughout subsequent reflectivity calculations. For an isolated surface reflectivity is reduced by the Nevot–Croce[36] factor, $\exp[-Q_R^2 \sigma_r^2]$, where σ_r is the surface roughness. At the maximum Q_R in our measurements, ~ 0.15 Å^{-1}, this smearing of the scattering length density profile reduces the calculated reflectivity in our fits by a factor of approximately one-half.

The variation in scattering length density profile giving rise to the peaks observed in the specular reflectivity was modeled using a simple damped cosine wave oscillation of the membrane volume fraction about the bulk value. The corresponding oscillation in the scattering length density above the surface layer is visible in the fit insets to the reflectivity data plots. The free parameters of this feature were the amplitude of the oscillation, $\Delta \phi_M$; its periodicity, d_z; decay depth, ξ_z; and the zero phase position, z_o, of the cosine wave oscillation taken from the center of the surface adsorbed layer. In the fitting procedure $\Delta \phi_M$ was constrained to prevent the pure heavy brine scattering length density being exceeded at the minimum membrane concentration over the oscillation. So the average membrane concentration in the solution has the form,

$$\phi[z] = \phi_M + \Delta \phi_M e^{-(z-z_o)/\xi_z} \cos[2\pi(z-z_o)/d_z]. \quad (10)$$

And the scattering length density in solution as a function of depth is then

$$\beta[z] = \phi[z] \beta_M + (1 - \phi[z]) \beta_{D_2O}. \quad (11)$$

This fitting model is a direct phenomenological analog of the fits to the bulk sponge data, since a Lorentzian is derived from the Fourier transform of an exponentially decaying oscillation.

Values of $R[Q_R]$ for these continuous functional scattering length density profiles were calculated by approximating them by a series of fine steps and solving for the dynamical multilayer neutron reflectivity by the methods described in detail by Russell[11] and Zhou et al.[10] (The scattering length density inset plots in Fig. 4 are calculation multilayer plots.) The calculated reflectivities were averaged over instrument resolution at each data point and fits to the data obtained by conventional χ^2 minimization.[37] The values of the parameters determined from the NR fits (ϕ_M, ϕ_s, $\Delta \phi_M$, z_o, d_z, and ξ_z) are shown in Table I.

V. DISCUSSION OF RESULTS

The local surface structure parameters derived from our NR measurements may be discussed in the well known context of membrane phase dilution behavior. It was observed by Porte et al.[4] that for a given sheet structure geometry in the bulk the characteristic correlation length d_c obtained from scattering results will be proportional to the sheet thickness and inversely proportional to volume fraction occupied by the sheets, for our system t_M and ϕ_M respectively. So,

$$d_c = \frac{2\pi}{Q_c} \equiv C \frac{t_M}{\phi_M}. \quad (12)$$

For the simplest situation to visualize, flat lamellar structures without ripples, d_c is simply the lamellar periodicity d_α, the sheets are as close as they can be and the geometrical constant of proportionality C is unity. Curvature and rippling of the sheet structure increases the value of C. For the stiff high symmetry case of a bicontinous cubic structure without ripples, for which the negative Gaussian curvature of the membranes is constant, C is about 1.5.[4,38] Ideal dilution behavior would be followed if the constant of proportionality for a given geometry did not change with concentration, keeping the experimentally measurable quantity $d_c\phi_M \equiv Ct_M$ constant with respect to concentration. However, for these systems thermodynamic fluctuations are an intrinsic feature of the oscillation forces that dominate the membrane interactions.[39] The excess membrane area taken up by fluctuations leads to an increase in C and thus $d_c\phi_M$. This excess area effect increases with dilution, since the greater available volume between membranes allows higher amplitude, longer wavelength fluctuations. For lamellar systems C is usually in the range 1–1.3. Sponge phases ($d_c = d_3$) are essentially disordered cubic phases. For this less geometrically regular and more flexible morphology, the reported range of values for C is somewhat below the cubic phase value, typically 1.2–1.4. Also, due to the instrinsic curvature of the sponge phase, the value is about 20%–30% higher than for lamellar phases at the same membrane volume fraction.

The second last column of Table I gives the ratio of the bulk sponge correlation distance $d_3 = 2\pi/Q_3$ determined by SANS and the local depth periodicity d_z in the proximity of the quartz surface determined from our NR measurements. At the lowest concentrations this ratio is unity within errors and as the membrane volume fraction increases the clear trend is to a significantly smaller periodicity being established in the proximity of the solid–solution interface. The ratio of 1.22 ± 0.05 for the 46 vol % sample is similar to that expected between d_3 and d_α for bulk sponge and lamellar phases at the same membrane volume fraction. Over the same range the decay of the oscillation expressed as the ratio of the decay constant to the surface periodicity ξ_z/d_z (Table I final column) increases by a factor of 4. This trend suggests that as the bulk membrane volume increases an at least quasi-lamellar ordering is established within a few hundred Å of the solid–solution interface.

We therefore used the sheet structure Eq. (12) to determine the experimental values of $d_3\phi_M \equiv C_3t_M$ from the pore correlation peaks observed for the bulk sponge by SANS (and NS-SANS), with the effective surface quantities $d_z\phi_M$ and $z_o\phi_M$. To allow comparison with a true lamellar phase ordering at similar membrane volume fractions we also include values of $d_\alpha\phi_M \equiv C_\alpha t_M$ for a parallel series of SANS determinations of lamellar phase periodicity in our CPCl–hexanol–heavy brine system. This L_α phase series has a mass ratio of hexanol to CPCl of 0.9, the positions of these samples in the phase diagram are indicated in Fig. 1. The variation of these values with the bulk membrane volume fraction for the dilution series are plotted in Fig. 5. Clearly, at low membrane volume fraction the local surface layering periodicity d_z corresponds to the bulk sponge correlation
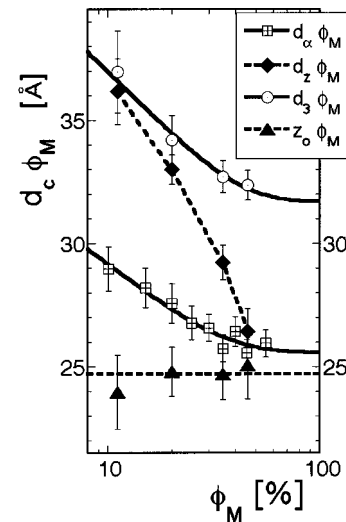

FIG. 5. Experimentally determined values of $d_c\phi_M$ vs ϕ_M for the sponge (dotted circles, $d_c = d_3$) and lamellar (crossed squares, $d_c = d_\alpha$) bulk phase dilution series. Solid line fits to the sponge and lamellar data are calculated using Eqs. (12) and the excess area Eq. (13) derived in Appendix D. Dilution scaled parameters $d_z\phi_M$ (solid diamonds) and $z_o\phi_M$ (solid triangles) are calculated from the period and zero phase position of the layered surface ordering for the sponge phase determined by NR.

peak, but approaches the periodicities measured for the lamellar systems at the same membrane volume fraction at higher concentrations.

The line fits to the sponge and lamellar plots of $d_c\phi_M \equiv Ct_M$ versus ϕ_M are adapted from the widely used treatment of Roux *et al.*[33] giving the thermodynamic corrections excess area effects in dilute lamellar systems. At low concentrations these fluctuations result in an increase in C proportional to $\ln[1/\phi_M]$. At the higher membrane volume fraction range covered by our sample series these fluctuations begin to be strongly suppressed by geometrical constraints and a simple dilution law behavior $d_\alpha\phi_M \approx C't_M = \text{const}$ begins to emerge. The scaling of the plot in Fig. 5 is chosen to emphasize this behavior. (A very striking example of this effect may also be seen in a high resolution x-ray study of lamellar systems reported by Freyssingeas *et al.*[40]) In our treatment, which is derived in Appendix D, the area coefficient C is described as the product of a purely geometric term for the phase in question, C', and a thermodynamic fluctuation term,

$$C \cong C'\left(1 + \frac{k_B T}{8\pi\kappa_o}\ln\left[1 + \frac{\kappa_o}{k_B T}\left(\frac{C't_M}{\Lambda_{\min}/x}\frac{(1-\phi_M)}{\phi_M}\right)^2\right]\right).$$
(13)

The fit to the fluctuation corrections to the area factor as a function of the membrane volume fraction ϕ_M depends on three parameters: κ_o/k_BT; the membrane's bare bending modulus in reduced thermodynamic units ($T = 295$ K); $C't_M$, the product of the geometric (zero fluctuation) value of the area factor and the membrane width; and $\Lambda_{\min}/x$, the short wavelength cutoff of the membrane fluctuations divided by a numerical factor $x \sim 1$. The fits shown in Fig. 5 use consistent values of $\kappa_o/k_BT \cong 0.8$, $t_M = 25.6 \pm 0.5$ Å, and

J. Chem. Phys., Vol. 116, No. 19, 15 May 2002

Sponge phases at a solid–solution interface   8541

$\Lambda_{\min}/x\sim50$ Å for both the sponge and lamellar fits. The geometrical area parameter for the sponge phase C'_3 was 1.25, assuming that the fluctuation suppressed value of the lamellar phase geometry $C'_\alpha\equiv1$. (Details of the fitting procedure are given in Appendix D.)

From Eq. (13) and the equivalent (D7) in Appendix D we can see that a change from dilute solution $\ln[1/\phi_M]$ dependence, equivalent to that observed by Roux et al.,[33] to a simple dilution law dependence as fluctuations are suppressed at higher concentrations will occur near a transition membrane volume fraction,

$$\phi_M^t\simeq\left(1+\sqrt{\frac{k_BT}{\kappa_o}\left(\frac{\Lambda_{\min}/x}{C't_M}\right)}\right)^{-1}. \quad (14)$$

This represents an estimate of when geometrical constraints on membrane oscillation due to inter-membrane collisions approaches the lower structural limit on membrane oscillation represented by $\Lambda_{\min}$. Using the parameters derived from our dilution fits for this system $\phi_M^t\sim30$ vol %. From Fig. 5 the transition between apparently spongelike local surface order to quasilamellar order apparently coincides with the crossing of this concentration regime. It may be speculated that as pressure due to membrane fluctuations decreases with concentration that the sponge structure is no longer stable against the ordering potential exerted by the solid surface.

Within the limits of our simple fitting profile, which models the local surface depth profile only in terms of its primary Fourier component and a simple exponential decay, the zero phase position of the local membrane concentration oscillation z_o represents an approximate indication of the center to center distance between the adsorbed surface layer and the average position of the first free membrane in solution. The scaled parameter $z_o\phi_M$ exhibits nearly ideal dilution behavior and is constant within errors about its mean value, 24.7 ± 0.6 Å, which is close to the surfactant membrane thickness $t_M=25.6\pm0.5$ Å determined from the lamellar phase dilution series. So the separation of this first solution layer from the surface is approximately the same as the periodicity we would expect in a lamellar phase without fluctuations at the same bulk membrane volume fraction. This suggests that in the structural accommodations necessary for the bulk sponge phase to conform to the surface constraints membrane fluctuations for this closest layer to the interface are suppressed at all concentrations.

It is interesting to (cautiously) correlate our results with the SFA measurements made on AOT sponges over a similar membrane volume fraction range by Antelmi et al.[8,9] (9–18 vol %) and Petrov et al.[7] (20–50 vol %). First, we note that we observe about the number of membrane concentration volume fraction oscillations in the surface constrained CPCl–hexanol sponge phases that one might expect from the SFA results on AOT sponges if we assume that the observed interactions begin to occur when surface ordered structures associated with the approaching solid surfaces begin to overlap significantly, i.e., there are about twice as many force steps as we observe distinct oscillations in the scattering length density insets in Fig. 4. Like our concentration oscillation decay constant normalized to the surface period-

icity ξ_z/d_z the number of these force steps (and therefore any presumed surface potential range normalized to step size) increased out of proportion to concentration increases. Petrov et al., for instance, observe only 3 force steps (with the last extremely weak) at 20 vol % and 8 at 40 vol %. In detailed measurements on series of 9–18 vol % AOT L_3 samples near the center of the sponge phase domain, like our series well away from the boundaries with adjacent biphasic regions, Antelmi et al.[9] observed the compressibility steps to be periodic at the L_3 periodicity. This is consistent with our observation of surface ordering periodicities d_z similar to the sponge phase correlation length d_3 at lower concentrations. Unfortunately their measurements did not extend to the higher concentrations at which we see d_z approach lamellar values. In future NR/NS-SANS studies we intend to compare the change of surface ordering with temperature[41] in the AOT system with the observed SFA interactions as phase boundaries are approached. It is also hoped that a "neutron confinement cell" currently under development[42] will eventually allow NR to routinely probe complex fluid structures formed between solid surfaces in close approach and thus directly address the question of confinement induced L_α/L_3 phase changes in AOT sponge systems.

VI. CONCLUSION

We have measured the local and near surface structure of bulk sponge phases of CPCl–hexanol in heavy brine under the constraint of a proximate quartz surface by simultaneous measurement of NR and the NS-SANS signal in the reflection plane on a neutron reflectometer with a one-dimensional position sensitive detector. The parameters derived from these measurements have been compared to those obtained from conventional bulk SANS on the sponge samples and a lamellar phase series covering the same range of membrane volume fractions.

No significant difference was found between the reduced NS-SANS and bulk SANS measurements for the sponge phases. This indicates that the surface conformation of the highly fluid sponge phase extends less than a few μm into the bulk. The NR results agree with this finding and are consistent with an adsorbed layer of membrane at the surface and a symmetric oscillation of the membrane volume fraction about the bulk value that is damped out within a few hundred Å of the surface for all our sponge samples. Obviously for any membrane fraction below 50 vol % (i.e., all our samples) this symmetric oscillation about the bulk value does not allow the membrane volume fraction in the solution to reach 100%, so this model precludes the formation of a true lamellar ordering with a number of fully occupied layers at the surface. We did explore a number of more complicated asymmetric models which allowed this to occur, as well as a number of other decay functions (including Gaussian and stretched exponential). None gave a satisfactory fit to our NR measurements.

At lower membrane volume fractions the surface layering periodicity we observed corresponds to the bulk sponge pore size correlation peak as determined from SANS and NS-SANS, but approaches the 25% smaller periodicities measured for lamellar systems at the same membrane vol-

ume fraction at higher concentrations. Over this same range of concentrations the bulk SANS dilution measurements for the lamellar and sponge systems indicate that membrane fluctuations are suppressed as geometric restrictions increasingly limit the longest wavelength mode the membrane structures can support. It is possible that this transition from a sponge-like to a quasilamellar local surface structure indicates that significant contributions to the local free energy from fluctuations are necessary to maintain the stability of a local spongelike ordering at the surface over an aligned lamellar ordering. The ideal lamellar dilution behavior of the zero phase position of the membrane concentration oscillation associated with the surface is apparently consistent with this interpretation. Since z_o represents an approximation of the distance from the surface adsorbed layer to the nearest free membranes in solution, this at least suggests that fluctuations are always suppressed for the closest membranes.[43]

This concentration dependence has a number of implications for models of the local surface ordering of the membranes. In the low concentration limit our observations suggest that such a model might well start from a picture of sponge phase with passages that are distorted or limited in direction in the proximity of the surface. On the other hand, the high concentration limit and the behavior of z_o might suggest a model starting from a lamellar phase which is increasingly defective with depth due to interlayer passages which finally reach the orientational disorder exhibited by sponge phase pores in the bulk. In either case, or in some alternative picture, the indications of a role for membrane fluctuation dynamics seem to indicate that a relatively sophisticated treatment will be necessary to determine the exact nature of the local surface ordering revealed by our measurements.

ACKNOWLEDGMENTS

APPENDIX A: NR/NS-SANS DATA REDUCTION

Full simultaneous reduction of NR/NS-SANS data sets in the current instrument configuration proceeds by analyzing the specular and off-specular signals in terms of the cross sections each represents. The total cross section of the measured specularly reflected neutron signal is related to the specular reflection coefficient R by

$$\sigma_R = R[Q_R[\alpha_i]] \times WL \sin \alpha_i \times \exp[-\mu_Q L_Q] \times f, \quad \text{(A1)}$$

where $WL \sin \alpha_i$ is the geometric acceptance of the quartz–solution interface of length L (80 mm for our cell), for a neutron illuminated sample width W (defined by a 19 mm $\hat{y}$ high guard slit at the sample's leading edge), at angle of incidence α_i; and $\exp[-\mu_Q L_Q]$ corrects for absorption as the neutron beam passes through the length L_Q of the quartz slab.

Since the instrument slits are parallel to $\hat{y}$ the beam collimation is loose in this direction and the specularly reflected beam can, and in the present case did, exceed the detector's 50 mm width somewhat. The factor f corrects for this, representing the fraction of the specularly reflected beam intercepted over the detector's 50 mm width. It is easily determined since by reorienting the detector's 100 mm length along $\hat{y}$ we can measure the specularly reflected beam over its full width in this direction (FWHM of 42 mm, 18 mm rms). The ratio of the reflected beam currents in this orientation to that in the normal $\hat{z}$ orientation gave a value $f = 0.71 \pm 0.04$ for the reflectometer configuration used this series of measurements.

Examination of Eq. (A1) shows that at angles of incidence below the critical angle for unit reflectivity (i.e., at angles of incidence $\alpha_i < \alpha_c$) the reflection cross section depends only on sample cell dimensions, the angle of reflection, the measured specular intensity fraction f, and the transmission through the full length of the quartz slab $\exp[-\mu_Q L]$. At a given incident neutron flux and cell geometry this allows us to directly obtain an absolute normalization of the cross section against the measured specularly reflected neutron currents. For the 11 and 20 vol % sponge samples the solution bulk scattering length density is greater than that of the quartz so a unit reflectivity region exists. The absolute normalization from these two samples $R=1$ regions agreed to within 3%. The averaged cross-section normalization (accurate to ~2%) was applied uniformly to the NR signals (between which uncertainty in the determination of f cancels out) and NS-SANS signals from all four samples.

The cross section per detector pixel in the off-specular signal from the near-surface bulk scattering is related to the differential macroscopic cross section for the in-solution scattering $d\Sigma_S/d\Omega'$ by[15]

$$\sigma_S \cong d\Sigma_S/d\Omega' \times \Delta\Omega_{\text{pixel}} (\sin \alpha_f / \sin \alpha_f')$$

$$\times \frac{WL^2}{2(\cot \alpha_i' + \cot \alpha_f')} \times \exp[-\mu_Q L_Q]$$

$$\times \frac{2((\mu_S - \mu_Q)L - 1 + e^{-(\mu_S - \mu_Q)L})}{(\mu_S - \mu_Q)^2 L^2}$$

$$\times (1 - R[Q_R[\alpha_i]])(1 - R[Q_R[\alpha_f]]). \quad \text{(A2)}$$

In this expression, the instrumental solid angle per detector pixel $\Delta\Omega_{\text{pixel}}$ (4.0×10^{-6} steradian) appearing in the first line is corrected for refraction as it crosses the solution–quartz interface to give the in-solution solid angle; the second line and third lines are a rearrangement of the effective scattering volume V_S' given previously in Eqs. (4) and (5); while the

final line is the correction for the transmission of the initial beam incident at α_i and transmission of the scattered beam back through the interface to exit at α_f.

Since the NS-SANS signal is a background signal to the specular reflectivity signal while its transmission correction includes specular reflectivities evaluated at α_i and α_f a full reduction of the NR/NS-SANS data set is necessarily an iterative procedure. In the present case the NS-SANS signal is much lower than the specular signal over the low α_i or α_f angle range for which the transmission correction is significant. Therefore the normalized reflectivity without background subtraction provides an adequate starting estimate for reflectivity values to be used for initial transmission corrections used in determinations of the NS-SANS signal.

For each data set the NS-SANS signal was evaluated over the off-specular angular regions on either side of the specular peak defined by $|\alpha_f - \alpha_i| \in [0.15°, 0.5°]$ along lines of constant Q'_z. The values of $d\Sigma_S/d\Omega'[Q'_z]$ determined from σ_S in these off-specular pixels were in turn used to improve the accuracy of the NS-SANS σ_S background estimates in the specular region, $(\alpha_f - \alpha_i) \simeq 0$, to improve the reflectivity determination. Likewise, the better determinations of the true specular cross section σ_R and specular reflectivity improve estimates of the bulk scattering length density and therefore the refraction corrected angles (α'_i and α'_f) necessary to evaluate the value of Q'_z at a given detector pixel and the corresponding value of $d\Sigma_S/d\Omega'$ from the expression for σ_S. For the data presented here this reduction procedure converged after only a couple of iterations. The reduced data presented here represents the third iteration of this procedure.

We note that the dependence of the NS-SANS signal σ_S represented by Eq. (A2), the consequences of which are seen in the data of Fig. 2(b), makes the use of so-called "longitudinal diffuse scans" an occasionally dubious method of determining nonspecular backgrounds to NR measurements. Often used in point detector reflectivity measurements, these consist of measuring the off-specular scattering at α_f equal to α_i plus an offset, i.e., at a different scattering vector, at a different effective scattering volume and at different interfacial transmissions to those pertaining for the nonspecular background at the position of the specular signal. The effects of the mismatch between background and specular signal will be particularly marked when relatively well defined strong bulk scattering features exist; as, for instance, in lamellar systems. Although in principle the results of such a scan could be corrected in a manner similar to that employed here to obtain a better estimate of the background to the specular signal, in practice it seems that this is rarely done. A similar point was made by Schlomka et al.[25] in their study of specular and diffuse scattering from Si/Ge layers.

The reduction procedure outlined above with transmission and resolution corrections applied as a function of wavelength is also applicable to time-of-flight neutron measurements.

APPENDIX B: ACCURACY OF ABSOLUTE NORMALIZATIONS FOR SANS AND NS-SANS

Full details of data collection and correction for instrumental backgrounds, etc. for the ORNL SANS instrument have been published in elsewhere.[27,44–48] For the conventional SANS measurements scattering intensities were converted to absolute differential cross sections by comparison with precalibrated secondary standards based on the measurement of beam flux, vanadium incoherent cross section, and the scattering from water and other reference materials.[44] For relatively strong scatterers such as ours, the $\pm 3\%$ uncertainty from this source is the major contribution to uncertainities in absolute normalization of conventional SANS data. The next highest in our case is determined by the accuracy of transmission corrections. For our samples $\delta T \sim 2\%$ for 2 mm thick sponge samples in standard fused silica SANS Hellma[49] cells. The measured transmissions simply scale measured SANS intensities and these uncertainties for both sample and scattering standard propagate directly through the normalization in the usual way. With smaller contributions from background and empty cell subtractions the absolute differential cross section uncertainty for these measurements is $\pm 4\%$.

In our NS-SANS measurements absolute cross section normalization to an accuracy of $\sim 2\%$ was possible using the $R=1$ specular reflection signal below the critical edge as a calibration standard. However, in this more complicated scattering geometry sample transmission measurements contribute a larger uncertainty in the final determination of the absolute differential cross section uncertainty than in conventional SANS. They contribute to the normalization through the appearance of total macroscopic cross sections, μ_S, calculated from them in the relatively complicated absorption correction dependence of the effective scattering volume V'_S of Eqs. (4) and (5) appearing on the second and third lines of Eq. (A2). The dependence on both the quartz slab transmission $\exp[-\mu_Q L]$ and incident beam width W appearing in the second line cancel out as common factors in the absolute normalization against the specular signals. To determine the transmission correction error we note that for all our samples $(\mu_S - \mu_Q)L \gg 1$ $\mu_S \gg \mu_Q$ so the sample absorption correction factor on the third line in Eq. (A2) is approximately equal to $2/\mu_S L$. Again a common factor L cancels out, and the dominant uncertainty in applying the absorption correction is simply $\delta(1/\mu_S)$. Transmission measurements at 2.59 Å on the reflectometer were made using the 2 mm Hellma cell bulk SANS samples. The uncertainty in the transmission measurement was again $\sim 2\%$. Since $\mu_S = -\ln[T]/t$, and ignoring uncertainties in the thickness t of the precision Hellma cells, we find that $\delta\mu_S/\mu_S \approx (\delta T/T)/\ln[T]$. For the $80 \pm 2\%$ transmission of the 11 vol % sample this uncertainty is $\pm 11\%$, while for the $60 \pm 2\%$ transmission of the 46 vol % sample it is $\pm 7\%$. The next largest contribution to the absolute normalization uncertainty is the 6% error in the specular interception fraction $f = 0.71 \pm 0.04$, which applies as a constant scaling factor to all four data sets. Other sample geometry contributions are accurate to a few percent. For the series the uncertainty in the absolute normalization with respect to comparing the SANS

8544   J. Chem. Phys., Vol. 116, No. 19, 15 May 2002

Hamilton *et al.*

and NS-SANS measurements varies from 9% to 12%.

APPENDIX C: ANALYTIC SPONGE FORM FACTOR APPROXIMATION

We begin with the one-dimensional form factor of an idealized infinite surfactant bilayer in solution. Over a thickness t the scattering length density contrast with the solvent is $\Delta\beta$. (In our case this thickness would be t_o, the hydrocarbon core width of the bilayer excluding the hydrated surface region.) With the bilayer centered at $z=0$ the form factor is

$$F^2[Q_z] = (\Delta\beta)^2 t^2 \, \mathrm{sinc}^2[Q_z t/2]. \tag{C1}$$

Following Nallet *et al.*,[50] we note that intensity from a real membrane structure is not actually zero at $Q_z = 2\pi/t$, and instead use their modified form,

$$F_N^2[Q_z] = 2(\Delta\beta)^2 \frac{(1 - \cos[Q_z t]\exp[Q_z^2\delta^2/2])}{Q_z^2}. \tag{C2}$$

which may be viewed as the result of an averaging of Eq. (C1) over a distribution of the layer thickness value about a mean t with Gaussian width δ. While the width could be a free parameter in the fitting procedure we found good correspondence with the numerical form factor of Lei *et al.*[28] with δ fixed at Nallet *et al.*'s value of $t/4$.

In cylindrical coordinates (r, θ, z) we can construct the three dimensional form factor of a "discoid" by letting the scattering length density contrast fall as $\exp[-r^2/\rho^2]$, where ρ is simply a transverse radius of gyration of the membrane's scattering length density contrast. The Nallet one-dimensional form factor is now simply multplied by the two-dimensional in-plane form factor,

$$F_{N3}^2[Q_r, Q_z] = F_N^2[Q_z](\pi\rho^2)^2 \exp[Q_r^2\rho^2/2]. \tag{C3}$$

Now $Q = \sqrt{Q_r^2 + Q_z^2}$. The scattering contrast volume corresponding to this form factor is $\langle V \rangle = \pi\rho^2\sqrt{t^2 + \delta^2}$ and its three-dimensional radius of gyration is given by $\langle R_g \rangle = \sqrt{\rho^2 + (t^2 + \delta^2)/12}$. Note that $\sqrt{t^2 + \delta^2}$ is simply the rms value of the contrast thickness over the distribution. Since for our choice of $\delta = t/4$ we have $\delta^2 \ll t^2$, we will simply approximate this rms width by t in the following expressions, so $V \cong \pi\rho^2 t$ and $R_g \cong \sqrt{\rho^2 + t^2/12}$.

At large scattering vector ($Q \gg 2\pi/\rho$ and $Q \gg 2\pi/t$) it is easy to obtain the average of random orientations of this form factor over the $4\pi Q^2$ surface of the Ewald sphere in reciprocal space,

$$\langle F_{N3}^2[Q] \rangle \cong F_N^2[Q](\pi\rho^2)^2 \frac{1}{Q^2\rho^2}. \tag{C4}$$

We note that at small scattering vector the familiar Guiner behavior for the form factor for an object of radius of gyration R_g and volume V is

$$F_G^2[Q] \cong (\Delta\beta)^2 V^2 \exp[-Q^2 R_g^2/3]. \tag{C5}$$

Examining Eqs. (C2) and (C4) we find that we can remove the $Q=0$ singularity and force the Guinier behavior of Eq. (C5) to second order in Q at small scattering vector

while maintaining the large scattering vector limit by a simple modification of the $1/Q^2\rho^2$ term in Eq. (C4). So,

$$\langle F_{N3}^2[Q] \rangle \cong F_N^2[Q](\pi\rho^2)^2 \frac{1}{Q^2\rho^2 + \exp[-2Q^2 R_g^2/3]}, \tag{C6}$$

which is the analytic form factor approximation used in the fits to the SANS data presented in Fig. 3. The behavior of this analytic form factor was found to be essentially equivalent to numerical calculations of the form factor used by Lei *et al.*[28] based on discs of radius R and thickness t, when the transverse radii of gyration for the two geometries were equal, i.e., $\rho = R/\sqrt{2}$.

APPENDIX D: EXCESS AREA FACTOR DERIVATION

The modified excess area factor for higher volume fraction fluctuating membrane systems presented as Eq. (13) of Sec. V was derived as follows. We express the constants C_3 and C_α as the product of a geometric factor describing the average membrane geometry without fluctuations C', and an excess area factor $A_{\mathrm{real}}/A_{\mathrm{proj}}$, the ratio of the real to projected bilayer area in a fluctuating membrane system. So,

$$C \equiv C'(A_{\mathrm{real}}/A_{\mathrm{proj}}). \tag{D1}$$

The Helfrich[33,51,52] expression for the excess area factor due to fluctuations may be put in the form,

$$\frac{A_{\mathrm{real}}}{A_{\mathrm{proj}}} \cong 1 + \frac{k_B T}{4\pi\kappa_o} \ln\left[\frac{\Lambda_{\mathrm{max}}}{\Lambda_{\mathrm{min}}}\right], \tag{D2}$$

where T is the absolute temperature and κ_o is the membrane's bending modulus. Λ_{max} and Λ_{min} are the long and short wavelength cutoffs of the membrane oscillations. The long wavelength cutoff is determined the limit at which the membrane can be considered to be freely fluctuating, i.e., unobstructed and not affected by collisions. At a particular temperature this limit will be reached when the average transverse excursion of the mode $x\sqrt{k_B T/\kappa_o}\Lambda_{\mathrm{max}}$ equals the average separation between the membrane surfaces. The constant of proportionality x is of order unity and model dependent. Using the estimation from the unified microscopic theory of dilute lamellar phases due to Golubović and Lubensky[53] would give a value $x = \sqrt{32/3\pi}/2 \approx 0.92$, while Pieruschka *et al.*[54] estimated $x \approx \sqrt{3}/2 \approx 0.86$.[55]

To first order we can approximate the membrane separation by its value in the absence of ripples (the rigid membrane limit, $A_{\mathrm{real}}/A_{\mathrm{proj}} \equiv 1$), which is simply

$$d_c[\kappa_o \gg k_B T] - C' t_M \cong C' t_M (1 - \phi_M)/\phi_M. \tag{D3}$$

Note the $(1 - \phi_M)$ factor arising from the correction of the center to center correlation distance between membranes for the transverse average of the finite bilayer thickness, $C' t_M$, for a given geometry. For dilute systems this factor is close to unity and may be neglected,[33] but as noted by Helfrich[52] should be retained for systems such as ours with ϕ_M not much less than unity. Simply using this expression for the separation gives the following first order estimate of the maximum,

$$\Lambda_{\max}|_o \approx x\sqrt{\kappa_o/k_BT}\,C't_M(1-\phi_M)/\phi_M. \qquad (D4)$$

While retaining the $(1-\phi_M)$ term in this expression ensures that it predicts the absence of room to oscillate as $\phi_M \to 1$, it gives an obviously unphysical limit of $\Lambda_{\max}/\Lambda_{\min} \to 0$, i.e., it allows $\Lambda_{\max}$ to be less than the short wavelength cutoff. The physically consistent limit is that as $\phi_M \to 1$ that $\Lambda_{\max}/\Lambda_{\min} \to 1$ (exactly) and thus $\ln[\Lambda_{\max}/\Lambda_{\min}] \to 0$. To modify this estimate to give this correct high membrane concentration limit, while retaining its correct dilute solution behavior, we can simply add it in quadrature to the short wavelength cutoff $\Lambda_{\min}$.[56] Thus we use

$$\Lambda_{\max} \cong \sqrt{(\Lambda_{\max}|_o)^2 + \Lambda_{\min}^2}. \qquad (D5)$$

Substituting these expressions we obtain

$$d_c\phi_M \equiv C't_M(A_{\text{real}}/A_{\text{proj}}), \qquad (D6)$$

and the estimate of the excess area factor becomes

$$\frac{A_{\text{real}}}{A_{\text{proj}}} \cong 1 + \frac{k_BT}{8\pi\kappa_o}\ln\left[1 + \frac{\kappa_o}{k_BT}\left(\frac{C't_M}{\Lambda_{\min}/x}\frac{(1-\phi_M)}{\phi_M}\right)^2\right]. \qquad (D7)$$

The fits to our dilution series data shown in Fig. 5 use Eqs. (D6) and (D7) to obtain best fit values for three independent fitting parameters, κ_o/k_BT, $C't_M$, and $\Lambda_{\min}/x$. For the 9 lamellar data points we obtained a value of $\kappa_o/k_BT = 0.8 \pm 0.2$, consistent with previous determinations by dilution law measurements.[33,34] The product of the geometric area factor and the membrane thickness was $C'_\alpha t_M = 25.6 \pm 0.5$ Å. If we simply set $C'_\alpha = 1$, i.e., the value for flat stacked membranes, this value maybe considered a direct measurement of the effective membrane thickness t_M in solution. As noted in Sec. IV this value is consistent with a hydrocarbon core width of $t_o = 20.5 \pm 1.0$ Å and a 2–3 Å head group surface layer thickness.

The best fit value obtained for $\Lambda_{\min}/x$ was 50 ± 25 Å. Using $x \sim 0.9$, our estimate of the short wavelength cutoff is then $\Lambda_{\min} \approx 45 \pm 22$ Å. The standard error limits on this value put it slightly higher than the usual estimates, which correspond to about twice the CPCl surfactant head group separation in the membrane,[33,34] which is only about 20 Å for this system.[57] However, that this value is approximately twice the membrane thickness is suggestive, as it represents twice the dimension of the minimal unit section of membrane governed by the fluctuation dynamics,[52] which would therefore be a slab of membrane of length $\sim t_M$ in all dimensions. Phenomenologically, this term simply acts as a cutoff value for the dynamics dominating membrane behavior at low concentrations and forces the required physically realistic constraint $\Lambda_{\max}/\Lambda_{\min} \to 1$ as $\phi_M \to 1$. Its effect is evident in our data as for membrane volume fractions above 30 vol% we begin to approach something like simple dilution law behavior, i.e., $d_c\phi_M \approx C't_M =$ const, in both membrane phase morphologies.

This supression of the logarithmic correction at higher concentrations has been observed previously. A striking example was reported by Freyssingeas *et al.*[40] in a high resolution x-ray measurements of lamellar phases in the $C_{12}E_5$–hexanol–water system at membrane concentrations up to 72 vol%. They found that $d_\alpha\phi_M$ was essentially constant at membrane concentrations above 50 vol% after falling by about by one third from its value at $\phi_M \sim 1$ vol%. They then used the simple dilution law at these higher concentrations to obtain the membrane thickness for this system (as we could for ours above 30 vol%). Similar ideal dilution law behavior for DMPC L_α phases at higher concentrations was noted and discussed by Demé *et al.*[58]

Since there only four data points in the sponge dilution series a three parameter fit will be overdetermined, making finite error estimation difficult. We therefore fixed $\Lambda_{\min}/x$ at 50 Å, the lamellar best fit value. For this fit κ_o/k_BT was 0.8 ± 0.3, indistinguishable from its value for the lamellar phase series, while $C'_3 t_M$ was 31.7 ± 0.7 Å. From this latter value and the membrane thickness value from the lamellar fit, $t_M = 25.6 \pm 0.5$ Å, we obtain an estimate of the zero fluctuation limit geometric area factor for the CPCl–hexanol–brine sponge phase of $C'_3 = 1.25 \pm 0.004$.

[1] P. G. de Gennes, Rev. Mod. Phys. **64**, 645 (1992).
[2] G. Porte, Curr. Opin. Colloid Interface Sci. **1**, 345 (1998).
[3] G. Porte, "From giant micelles to fluid membranes" in *Soft Matter Physics*, edited by M. Daoud and C. E. Williams (Springer-Verlag, Berlin, 1999), Chap. 5, p. 155.
[4] G. Porte, J. Marignan, P. Bassereau, and R. May, J. Phys. (France) **49**, 511 (1988); G. Porte, J. Appell, P. Bassereau, and J. Marignan, *ibid.* **50**, 1335 (1989); Similar measurements were also reported by D. Gazeau, A. M. Belloocq, D. Roux, and T. Zemb, Europhys. Lett. **9**, 447 (1988).
[5] Freeze fracture microscopic imaging of the bilayer morphology by S. Strey, W. Jahn, G. Porte, and P. Bassereau, Langmuir **6**, 1635 (1990); The bicontinuous structure was also suggested on theoretical grounds by M. E. Cates, D. Roux, D. Andelman, S. T. Milner and S. A. Safran, Europhys. Lett. **5**, 733 (1988).
[6] R. Evans and M. M. Marcini, J. Chem. Phys. **86**, 7138 (1987).
[7] P. A. Petrov, U. Olsson, H. Cristenson, S. Miklavic, and H. Wennerström, Langmuir **10**, 988 (1994).
[8] D. A. Antelmi, P. Kekicheff, and P. Richetti, J. Phys. II **5**, 103 (1995).
[9] D. A. Antelmi, P. Kekicheff, and P. Richetti, Langmuir **15**, 7774 (1999).
[10] X.-L. Zhou, L.-T. Lee, S.-H. Chen, and R. Strey, Phys. Rev. A **46**, 6479 (1992). The similarity arises in that the membrane boundary between the separated solvent volumes in the sponge phase corresponds to the boundary between the oil and water volumes of the bicontinuous microemulsion phase.
[11] T. P. Russell, Mater. Sci. Rep. **5**, 171 (1990).
[12] J. Penfold and R. K. Thomas, J. Phys.: Condens. Matter **2**, 1369 (1990).
[13] W. A. Hamilton, P. D. Butler, S. M. Baker, G. S. Smith, J. B. Hayter, L. J. Magid, and R. Pynn, Phys. Rev. Lett. **72**, 2219 (1994).
[14] S. M. Baker, G. S. Smith, P. D. Butler, J. B. Hayter, W. A. Hamilton, R. Pynn, and L. J. Magid, Rev. Sci. Instrum. **65**, 412 (1994).
[15] W. A. Hamilton, P. D. Butler, J. H. Hayter, L. J. Magid, and P. J. Kreke, Physica B **221**, 309 (1996).
[16] P. D. Butler, W. A. Hamilton, L. J. Magid, J. B. Hayter, T. M. Slawecki, and B. Hammonda, Faraday Discuss. **104**, 65 (1996); **104**, 88 (1996).
[17] P. D. Butler, L. J. Magid, W. A. Hamilton, J. B. Hayter, B. Hammouda, and P. J. Kreke, J. Phys. Chem. **100**, 442 (1996).
[18] W. A. Hamilton, P. D. Butler, L. A. Magid, Z. Han, and T. M. Slawecki, Phys. Rev. E **60**, R1146 (1999).
[19] W. A. Hamilton, J. B. Hayter, and G. S. Smith, J. Neutron Res. **2**, 1 (1994).
[20] M. Yethiraj and J.A. Fernandez-Baca, in Materials Research Society Symposium Proceedings **376**, Neutron Scattering in Materials Science II, edited by D. A. Neuman, T. P. Russell, and B. J. Wuensch, 1995.
[21] ORDELA 1150N, Oak Ridge Detector Laboratory Inc., Oak Ridge, Tennessee.
[22] A. G. Klein and S. A. Werner, Rep. Prog. Phys. **46**, 259 (1986).
[23] S. K. Sinha, E. B. Sirota, S. Garoff, and H. B. Stanley, Phys. Rev. B **38**, 2297 (1988).

8546   J. Chem. Phys., Vol. 116, No. 19, 15 May 2002

Hamilton *et al.*

[24] J.-P. Schlomka, M. Tolan, L. Schwalowsky, O. H. Seeck, J. Stettner, and W. Press, Phys. Rev. B **51**, 2311 (1995).

[25] By tighter collimation in the $\hat{y}$ direction it would be possible to improve the Q_y resolution, though not to any dramatic degree due to the effect of the 50 mm detector pixel width; and also make the specular beam fall fully within this width, eliminating the need to apply the specular interception fraction f correction in Eq. (A1). However, the ray optics of our instrument configuration shows that this will also greatly reduce the possible incident neutron current on the sample cell area and hence the strength of the NR and NS-SANS signals.

[26] The substitution of D_2O to increase neutron contrast alters the phase behavior very little from that for light water [H. F. Mahjoub, K. M. McGrath, and M. Kléman, Langmuir **12**, 3131 (1996)], lowering the hexanol to CPCl mass ratios of the L_3 phase region by only a few percent.

[27] This instrument has been shortened from the 30 m geometry described in W. C. Koehler, Physica B **137**, 320 (1986) and used in the measurements reported in Refs. 44–48. The collimator length of the new geometry is 4.5 m and the maximum sample to detector distance is now 7.5 m, down from 18 m. Otherwise the instrument's operation and data correction procedures remain unchanged.

[28] N. Lei, C. R. Safinya, D. Roux, and K. S. Liang, Phys. Rev. E **56**, 608 (1997).

[29] D. Roux, M. E. Cates, U. Olsson, R. G. Ball, F. Nallet, and A. M. Bellocq, Europhys. Lett. **11**, 229 (1990).

[30] D. Roux, C. Coulon, and M. E. Cates, J. Phys. Chem. **96**, 4147 (1992).

[31] J. C. Schulz, G. G. Warr, P. D. Butler, and W. A. Hamilton, Phys. Rev. E **63**, 041604 (2001), and references therein; B. H. Bijsterbosch, J. Colloid Interface Sci. **47**, 186 (1973).

[32] L. Porcar, W. A. Hamilton, P. D. Butler, and G. G. Warr (in preparation).

[33] D. Roux, F. Nallet, É Freyssingeas, G. Porte, P. Bassereau, M. Souri, and J. Marignan, Europhys. Lett. **17**, 575 (1992).

[34] G. Bouglet and C. Ligoure, Eur. Phys. J. B **9**, 137 (1999); and G. Bouglet (private communication).

[35] R. Gomati, J. Appell, P. Bassereau, J. Marignan, and G. Porte, J. Phys. Chem. **91**, 6203 (1987).

[36] L. Nevot and P. Croce, Rev. Phys. Appl. **15**, 761 (1980).

[37] The fitting program used for this data is an eponymous integral data collection and analysis package for the MIRROR neutron reflectometer developed by J. B. Hayter and W. A. Hamilton (1992–2001). The statistical and error estimation concepts used therein are described in P. R. Bevington, *Data Reduction and Error Analysis for the Physical Sciences* (McGraw–Hill, New York, 1969), Chap. 11; W. H. Press, S. A. Teukolsky, W. T. Vetterling, and B. P. Flannery, *Numerical Recipes in Pascal* (Cambridge University Press, Cambridge, 1989), Chap. 15. The minimization routine employed by the MIRROR program is the "downhill simplex" method of J. A. Nelder and R. Mead, Comput. J. (UK) **7**, 308 (1965), in an implementation described in Chapter 10, Sec. 4 of *Numerical Recipes*.

[38] I. S. Barnes, S. T. Hyde, B. W. Ninham, P. J. Derian, M. Drifford, G. G. Warr, and Th. Zemb, Prog. Colloid Polym. Sci. **1**, 358 (1988); Th. Zemb, Colloids Surf., A **129–130**, 435 (1997); I. Grillo, P. Levitz, and Th. Zemb, Eur. Phys. J. E **5**, 377 (2001) gives a value of 1.46.

[39] W. Helfrich, Z. Naturforsch. A **33**, 305 (1978). The range of electrostatic interactions between membranes in our samples is less than the 6.8 Å Debye screening length of the 0.2 M NaCl heavy brine solvent and thus much less than the membrane separation for our most concentrated samples. Thus undulation forces dominate intermembrane interactions in our study.

[40] É. Freyssingeas, F. Nallet, and D. Roux, Langmuir **12**, 6028 (1996).

[41] Increasing temperature in the AOT systems (M. Skouri Ph.D. thesis, University of Montpellier, 1990) has a similar effect to decreasing the mass ratio m_{Hex}/m_{CPCl} in the CPCl–hexanol sponges. While the temperature stability of the CPCl–hexanol sponges has an advantage in the development of the techniques presented in the current study, this temperature sensitivity of AOT sponge phases obviously allows a much more experimentally convenient and reliable approach to the $L_3/L_\alpha+L_3$ phase boundary than changing the membrane composition.

[42] T. L. Kuhl, G. S. Smith, J. N. Israelachvili, J. Majewski, and W. A. Hamilton, Rev. Sci. Instrum. **72**, 1715 (2001).

[43] If we examine the bulk phase diagram for this system (Fig. 1) we see that increasing the mass ratio m_{Hex}/m_{CPCl} increases the intrinsic curvature of the membrane phases in this system. It should be noted that changes in membrane curvature due to the static and dynamic constraints imposed by proximity to the surface may therefore in their turn be expected to alter the membrane composition. Any such effect would be strongest for the layers nearest the surface which are those probed by NR in our study. However, changing the ratio of the hydrogenous components does not significantly alter the membrane's scattering length density or its neutron contrast with respect to the heavy brine solvent or the quartz. Consequently our NR results for the membrane volume fraction variation in this region would be essentially unaffected. We are currently unaware of any experimental method with the local specificity or sensitivity necessary to explore this intriguing possibility.

[44] G. D. W. Wignall and F. S. Bates, J. Appl. Crystallogr. **20**, 28 (1986).

[45] S.-H. Chen and T. L. Lin, "Colloidal Solutions," in *Methods of Experimental Physics,* edited by D. L. Price and K. Sköld (Academic, New York, 1987), Vol. 23B, Chap. 16, p. 489.

[46] R. G. Alamo, J. D. Londono, L. Mandelkern, F. C. Stehling, and G. D. Wignall, Macromolecules **27**, 411 (1994).

[47] J. D. Londono, A. H. Narten, G. D. Wignall, K. G. Honnell, E. T. Hsieh, T. W. Johnson, and F. S. Bates, Macromolecules **27**, 2864 (1994).

[48] C. T. Lee, Jr., P. A. Psathas, K. J. Ziegler, K. P. Johnston, H. J. Dai, H. D. Cochran, Y. B. Melnichenko, and G. D. Wignall, J. Phys. Chem. B **104**, 11 094 (2000).

[49] Hellma Cells, Inc., Plainview, New York; and Hellma GmbH, Müllheim, Germany.

[50] F. Nallet, R. Laversanne, and D. Roux, J. Phys. II **3**, 487 (1993).

[51] W. Helfrich and R. N. Servuss *et al.*, Nuovo Cimento D **3**, 137 (1984).

[52] W. Helfrich, J. Phys.: Condens. Matter **6**, A79 (1994).

[53] L. Golubović and T. C. Lubensky, Phys. Rev. B **39**, 12 110 (1989).

[54] P. Pieruschka, S. Marcelja, and M. Teubner, J. Phys. II **4**, 763 (1994).

[55] The factors of 1/2 included here explicitly arise since the coefficients appearing in Refs. 53 and 54 use the mean distance between collisions as a scale length which is $\Lambda_{max}/2$.

[56] Comparing our treatment here with that of Helfrich (Ref. 52) we may identify $\Lambda_{max}^2/\Lambda_{min}^2$ as the local count of the number of connected but unobstructed (i.e., between collisions) minimal membrane sections (Helfrich's "$N/2$") expressed as a ratio of areas. The addition in quadrature here simply ensures that this count has a physically consistent limit of unity rather than zero as $\phi_M \rightarrow 1$.

[57] The analogy with the acoustic phonon scattering limit is taken from hard condensed matter, where the maximum phonon wave vector is equal to $\pi/a = 2\pi/\Lambda_{min}$, where a is size of the unit cell, the minimal building block of the crystalline structure. [See, for instance, N. W. Ashcroft and N. D. Mermin, *Solid State Physics* (Holt, Rinehart, and Winston, Philadelphia, 1976), Chaps. 22 and 23.] So $\Lambda_{min} = 2a$. In our system a *lower limit* for the analogous unit cell size will correspond approximately to the separation of CPCl head groups in the surface of the membrane. For both sponge and lamellar phases considered here there are about 3 hexanol molecules for each CPCl molecule (2.68 for the lamellar phase and 3.20 for the sponge). Using a value of 3 and the molecular volume of CPCl (608 Å^3) and hexanol (212 Å^3) and the membrane thickness $t_M = 25.6$ Å derived from our lamellar phase fits the area per head group on the surface is about 100 Å^2. We can estimate the lower limit of a as the square root of this number or about 10 Å, corresponding to the 20 Å estimate for Λ_{min} given in the body of the text. Note, that the value of a used to estimate the fluctuation wavelength cutoff should not, as is sometimes assumed, be the minimum separation of *any* two molecules in the membrane plane, it is necessarily an estimate of the minimum size of the effective structural unit in the plane of the membrane. This structural unit and the minimum wavelength mode it supports could be larger than the CPCl head group separation if the system were, for instance, structurally corrugated on some length scale. The exploration of this observation is beyond the scope of this paper.

[58] B. Demé, M. Dubois, Th. Zemb, and B. Cabane, J. Phys. Chem. **100**, 3828 (1996).